

LETTERS

Quantum simulation of frustrated Ising spins with trapped ions

K. Kim¹, M.-S. Chang¹, S. Korenblit¹, R. Islam¹, E. E. Edwards¹, J. K. Freericks², G.-D. Lin³, L.-M. Duan³ & C. Monroe¹

A network is frustrated when competing interactions between nodes prevent each bond from being satisfied. This compromise is central to the behaviour of many complex systems, from social¹ and neural² networks to protein folding³ and magnetism^{4,5}. Frustrated networks have highly degenerate ground states, with excess entropy and disorder even at zero temperature. In the case of quantum networks, frustration can lead to massively entangled ground states, underpinning exotic materials such as quantum spin liquids and spin glasses^{6–9}. Here we realize a quantum simulation of frustrated Ising spins in a system of three trapped atomic ions^{10–12}, whose interactions are precisely controlled using optical forces¹³. We study the ground state of this system as it adiabatically evolves from a transverse polarized state, and observe that frustration induces extra degeneracy. We also measure the entanglement in the system, finding a link between frustration and ground-state entanglement. This experimental system can be scaled to simulate larger numbers of spins, the ground states of which (for frustrated interactions) cannot be simulated on a classical computer.

Linus Pauling predicted in 1945 that the frustrated oxygen–hydrogen bond lengths in the pyrochlore lattice of ice would lead to a macroscopic degeneracy of the ground state near zero temperature¹⁴. This zero-point entropy has been observed in spin-ice materials^{5,15}, where the competing interactions are magnetic in nature. In the simple case of a two-dimensional triangular lattice with frustrated antiferromagnetic Ising interactions, the ground-state degeneracy can easily be seen (Fig. 1a): only two of the three spins on each triangular cell can align antiparallel, so all possible mixed configurations in each triangle (three-quarters of all cases) are ground states. Quantum superposition of these degenerate states leads to massive entanglement that is important in our understanding of the complex phase structure of many frustrated materials, ranging from molecular and liquid crystals to high-temperature superconductors^{5,16}.

In our experiment, we implement a quantum simulation of the smallest possible frustrated magnetic network, which consists of three spins. This work builds on earlier results for two trapped ions¹², in a system that can be scaled to much larger numbers of spins. We control the sign and strength of the individual magnetic interactions, directly measure all possible spin correlation functions and characterize entanglement using techniques borrowed from quantum information science^{12,17}. The experiment is based on a linear chain of three trapped atomic ¹⁷¹Yb⁺ ions, where the effective spin-1/2 system is represented by the ²S_{1/2} |*F* = 1, *m_F* = 0⟩ and |*F* = 0, *m_F* = 0⟩ hyperfine ‘clock’ states in each ion, depicted by |↑⟩_z and |↓⟩_z, respectively¹⁸, and separated in frequency by $\nu_{\text{HF}} = 12.642821$ GHz.

The ions are confined in a three-layer linear trap¹³ and form a crystal along the trap’s *z* axis with a centre-of-mass trap frequency of $\nu_z = 1.49$ MHz. The three normal modes of transverse motion along the principal *x* axis occur at frequencies $\nu_1 = 4.334$ MHz,

$\nu_2 = 4.074$ MHz and $\nu_3 = 3.674$ MHz. Off-resonance laser beams uniformly illuminate the ions, driving stimulated Raman transitions between the spin states and also imparting spin-dependent forces in the *x* direction. As discussed in Methods, this allows quantum simulation of the Ising Hamiltonian with a transverse field^{10–12}

$$H = \sum_{i < j} J_{i,j} \sigma_x^{(i)} \sigma_x^{(j)} + B_y \sum_i \sigma_y^{(i)} \quad (1)$$

where B_y is an effective uniform transverse magnetic field with each spin having unit magnetic moment, and we have set Planck’s constant, \hbar , equal to one. For three spins, we define $J_1 \equiv J_{1,2} = J_{2,3}$ as the nearest-neighbour interaction and $J_2 \equiv J_{1,3}$ as the next-nearest-neighbour interaction (Fig. 1b), and $\sigma_x^{(i)}$ denote the Pauli matrices of the *i*th spin. We initialize each spin parallel to a strong transverse field and then adiabatically lower the field relative to the Ising couplings so that the

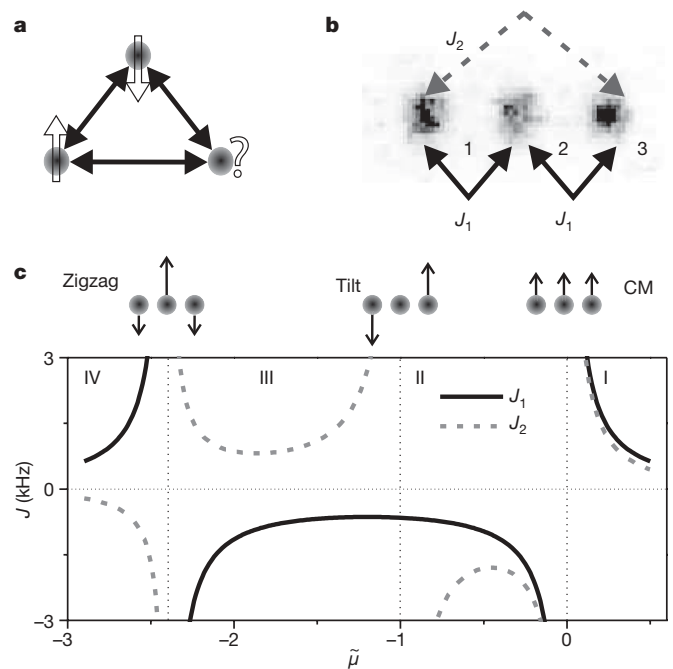


Figure 1 | Frustrated Ising spins. **a**, Simplest case of spin frustration, with three antiferromagnetic spins on a triangle. **b**, Image of three trapped atomic ¹⁷¹Yb⁺ ions in the experiment, taken with an intensified charge-coupled-device camera, with nearest-neighbour (J_1) and next-nearest-neighbour (J_2) interactions. **c**, Expected form of the Ising interactions J_1 and J_2 , controlled through the detuning, $\tilde{\mu}$, of an optical spin-dependent force, scaled to the axial (ν_z) and transverse (ν_1) centre-of-mass (CM) normal-mode frequencies of motion such that the CM, tilt and zigzag modes of transverse motion occur at $\tilde{\mu} \equiv (\mu^2 - \nu_1^2)/\nu_z^2 = 0, -1$ and -2.4 , respectively¹³.

¹Joint Quantum Institute, University of Maryland Department of Physics and National Institute of Standards and Technology, College Park, Maryland 20742, USA. ²Department of Physics, Georgetown University, Washington DC 20057, USA. ³MCTP and Department of Physics, University of Michigan, Ann Arbor, Michigan 48109, USA.

quantum state ideally follows the ground state of the Hamiltonian in equation (1). Because the transverse field does not commute with the Ising couplings, it provides a quantum interaction that leads to an entangled ground state^{7,8}.

As shown in Fig. 1c, we have nearly complete control of the signs and strengths of J_1 and J_2 through μ , the detuning of the lasers from spin resonance, which regulates the Coulomb interaction between the ions by coupling to particular collective modes of motion^{19,20}. In detuning regions II and IV in Fig. 1c, the next-nearest-neighbour interaction is ferromagnetic, because $J_2 < 0$. The resulting ground state as $B_y \rightarrow 0$ is an entangled superposition of the two states $|\downarrow\downarrow\downarrow\rangle$ and $|\uparrow\uparrow\uparrow\rangle$ in region II and $|\downarrow\uparrow\downarrow\rangle$ and $|\uparrow\downarrow\uparrow\rangle$ in region IV. (We define the default basis of spins to be along the x axis of the Bloch sphere: $|\uparrow\rangle \equiv |\uparrow\rangle_z + |\downarrow\rangle_z$ and $|\downarrow\rangle \equiv |\downarrow\rangle_z - |\uparrow\rangle_z$.) In regions I and III, the three spins are frustrated because $J_2 > 0$. In region I, all the interactions are antiferromagnetic and the Ising ground state is an entangled superposition of six states: the four antiferromagnetic asymmetric states $|\downarrow\downarrow\uparrow\rangle$, $|\uparrow\downarrow\downarrow\rangle$, $|\downarrow\uparrow\uparrow\rangle$ and $|\uparrow\uparrow\downarrow\rangle$, and the two antiferromagnetic symmetric states $|\downarrow\uparrow\downarrow\rangle$ and $|\uparrow\downarrow\uparrow\rangle$. Region III is more complicated, as it features a competition between the ferromagnetic nearest-neighbour interaction ($J_1 < 0$) and the antiferromagnetic next-nearest-neighbour interaction ($J_2 > 0$), and shows a type of frustration similar to that expected in two-dimensional ‘Union Jack’ lattices²¹.

The experiment proceeds as follows. We cool all transverse x modes to near their zero point of motion, and deep within the Lamb–Dicke regime, and then initialize the electronic states of each $^{171}\text{Yb}^+$ ion along the $-y$ axis of the Bloch sphere through optical pumping and rotation operations¹⁸. Next, we apply the Ising coupling along with a strong transverse field and adiabatically ramp down the field

(Methods). Finally, we measure the spins along the x axis of the Bloch sphere by rotating the spins from the x basis to the z basis and measuring the spin state ($|\downarrow\rangle_z$ or $|\uparrow\rangle_z$) by standard spin-dependent fluorescence techniques¹⁸ using a charge-coupled-device imager (the detection efficiency is $\sim 95\%$ per spin, including initialization and rotation errors). We determine the probability of each spin configuration (for example $P_{\downarrow\uparrow\uparrow}$) by repeating the above procedure $\sim 1,000$ times. We also measure the number of spins in state $|\uparrow\rangle$ by using a photomultiplier tube, which is useful for higher-efficiency measurements of certain symmetric observables such as entanglement fidelities and witness operators.

The above simulation is performed for various magnetic field end points, B_y , and laser beat-note detunings, μ . Figure 2a shows the expected ferromagnetic order of the exact ground state, characterized by $P_{\downarrow\downarrow\downarrow} + P_{\uparrow\uparrow\uparrow}$ and calculated by diagonalizing equation (1). The observed evolution of all eight spin states is shown in Fig. 2b–f for various values of μ . The cases in Fig. 2b, d, e correspond to situations in which the underlying Hamiltonian is frustrated, which is reflected in the large number of states with roughly equal probability at the end of the ramps when $B_y \ll J_{\text{rms}} \equiv \sqrt{(2J_1^2 + J_2^2)}/3$. The theoretical curves show both the exact ground-state populations as well as the population evolution expected from the applied time-dependent Hamiltonian²², using the Trotter formula and including the contribution from phonons to lowest order in the Lamb–Dicke expansion²³. The case in Fig. 2b corresponds to nearly uniform antiferromagnetic couplings and gives roughly equal probabilities for all six antiferromagnetic states (three-quarters of all possible spin states). Figure 2d shows a situation in which the four asymmetric antiferromagnetic

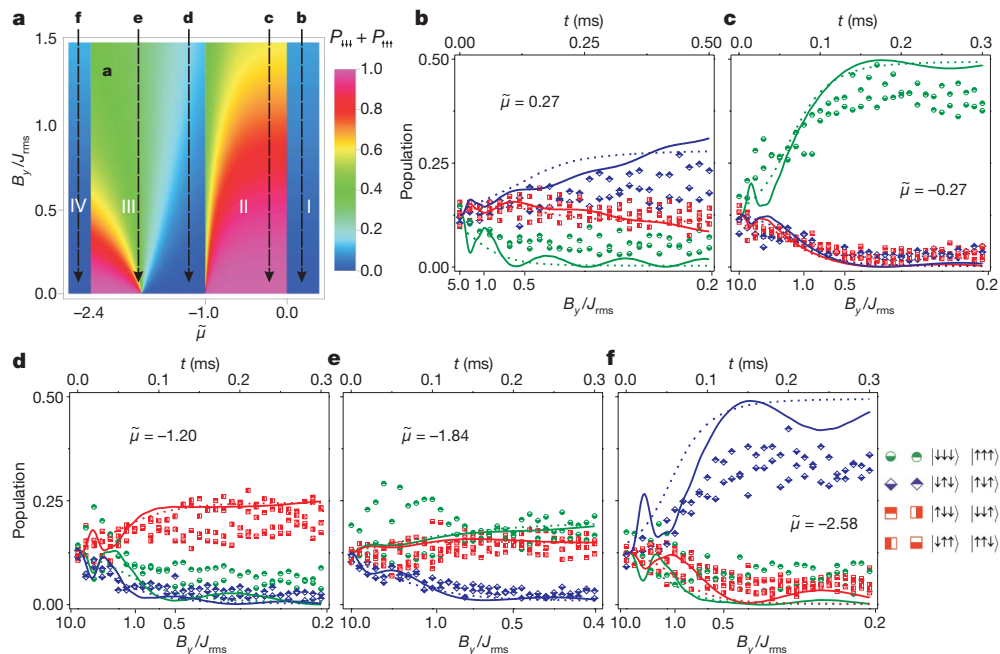


Figure 2 | Quantum simulation of the three-spin Ising model with a transverse field. **a**, Theoretical phase diagram of ferromagnetic order of the Ising model with a transverse field, characterized by $P_{\downarrow\downarrow\downarrow} + P_{\uparrow\uparrow\uparrow}$ plotted as a function of the final value of B_y/J_{rms} and the scaled laser beat-note detuning, $\tilde{\mu}$. **b–f**, Evolution of each of the eight spin states, measured with a charge-coupled-device camera, plotted as B_y/J_{rms} is ramped down in time, with each plot corresponding to a different form of the Ising couplings through the laser detuning (trajectories denoted by vertical dashed lines in **a**). The green circles are the two ferromagnetic states, the blue diamonds are the two symmetric antiferromagnetic states and the red squares are the remaining four asymmetric antiferromagnetic states. The dotted lines correspond to the populations in the exact ground state and the solid lines represent the theoretical evolution expected from the actual ramp, including non-adiabaticity from the initial sudden switch-on of the Ising Hamiltonian. The probability of inelastic spontaneous scattering is not included in the

theoretical curves. **b**, All interactions are antiferromagnetic (region I of Fig. 1c). The ferromagnetic-ordered states vanish and the six antiferromagnetic states are all populated as $B_y \rightarrow 0$. Because $J_2 \approx 0.8J_1$ for this data, a population imbalance also develops between symmetric and asymmetric antiferromagnetic states. **c**, All interactions are ferromagnetic (region II of Fig. 1c), with evolution to the two ferromagnetic states as $B_y \rightarrow 0$. **d**, Strong antiferromagnetic interactions between next-nearest neighbours and weak ferromagnetic interactions between nearest neighbours. Here the four asymmetric antiferromagnetic states $|\downarrow\downarrow\uparrow\rangle$, $|\uparrow\downarrow\downarrow\rangle$, $|\downarrow\uparrow\uparrow\rangle$ and $|\uparrow\uparrow\downarrow\rangle$ emerge with roughly equal probabilities. **e**, Next-nearest-neighbour antiferromagnetic interactions balance nearest-neighbour ferromagnetic interactions, with six states emerging. **f**, Nearest-neighbour antiferromagnetic interactions and next-nearest-neighbour ferromagnetic interactions, with states $|\downarrow\uparrow\downarrow\rangle$ and $|\uparrow\downarrow\uparrow\rangle$ emerging.

states emerge (half of all states), and the non-frustrated cases in Fig 2c, f show only two states emerging, owing to the global spin parity symmetry of the Hamiltonian in equation (1).

The adiabatic evolution of the ground state of equation (1) from $B_y \gg J_{\text{rms}}$ to $B_y \ll J_{\text{rms}}$ should result in an equal superposition of all Ising ground states and should therefore carry entanglement. For instance, in the ferromagnetic case with $J_1 < 0$ and $J_2 < 0$, we expect a Greenberger–Horne–Zeilinger (GHZ) ground state $|\downarrow\downarrow\downarrow\rangle - |\uparrow\uparrow\uparrow\rangle$. For the isotropic antiferromagnetic case with $J_1 = J_2 > 0$, we expect the ground state to be $|\uparrow\uparrow\downarrow\rangle + |\downarrow\downarrow\uparrow\rangle + |\uparrow\downarrow\uparrow\rangle - |\downarrow\uparrow\downarrow\rangle - |\uparrow\downarrow\downarrow\rangle - |\downarrow\uparrow\uparrow\rangle$, which is a superposition of two W states¹⁷. To compare these two cases, we characterize the entanglement in the system at each point in the adiabatic evolution by measuring particular entanglement witness operators, with negative expectation values indicating the corresponding form of entanglement¹⁷. For the ferromagnetic case, we measure the GHZ witness operator^{17,24}, $W_{\text{GHZ}} = 9/4 - \hat{J}_x^2 - \sigma_\phi^{(1)} \sigma_\phi^{(2)} \sigma_\phi^{(3)}$, where $\hat{J}_x \equiv \sum_i \sigma_x^{(i)}/2$ is proportional to the projection of the total effective angular momentum of the three spins along the x -direction, and ϕ is a direction in the y - z plane of the Bloch sphere. For the antiferromagnetic (frustrated) case, we measure the symmetric W-state witness operator¹⁷, $W_W = 4 + \sqrt{5} - 2(\hat{J}_y^2 + \hat{J}_z^2)$. In both cases, as shown in Fig. 3, we find that entanglement of the corresponding form develops during the adiabatic evolution. In this antiferromagnetic–ferromagnetic comparison, we operate with $\bar{\mu} \approx 0.22$ for both cases ($J_2 \approx 0.8J_1 > 0$), but for the ferromagnetic case we reverse the sign of B_y and follow the highest excited state¹², which is formally equivalent to measuring the ground state of the sign-inverted Hamiltonian.

In macroscopic systems, the global symmetry in the Ising Hamiltonian of equation (1) is spontaneously broken, and ground-state entanglement originating from this symmetry is expected to vanish for the non-frustrated ferromagnetic case⁷. However, for the frustrated antiferromagnetic case, the resultant ground state after symmetry breaking (for example $|\uparrow\uparrow\downarrow\rangle + |\uparrow\downarrow\uparrow\rangle + |\downarrow\uparrow\uparrow\rangle$) is still entangled. Although spontaneous symmetry breaking does not occur in a small system of three spins, we can mimic its effect by adding a

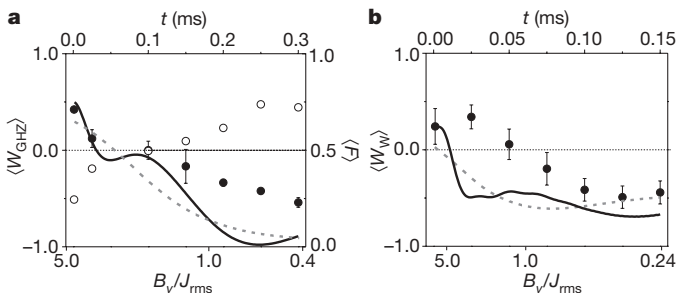


Figure 3 | Entanglement generation through the quantum simulation. Comparison of entanglement witness-operator measurements, using a photomultiplier tube for detection (see Methods for the error budgets), for ferromagnetic (a) and antiferromagnetic (b) situations as $|B_y|/J_{\text{rms}}$ is ramped down, with a negative value of the witness operator indicating entanglement. For this data, $|J_2/J_1| \approx 0.85$. Angle brackets indicate expectation values. **a**, In the ferromagnetic regime, we measure a GHZ witness operator with $\phi = y$ (filled circles) and find that entanglement occurs for $|B_y|/J_{\text{rms}} < 1.25$. The GHZ fidelity, F (open circles), or the overlap probability with the ideal GHZ state, is also extracted from this measurement, where $F > 0.5$ indicates entanglement²⁴. **b**, For the frustrated antiferromagnetic case, we measure a W-state witness operator (filled circles) and find that entanglement emerges for $B_y/J_{\text{rms}} < 1.1$. In both **a** and **b**, the dashed lines are theoretical witness-operator values for the exact ground states, and the solid lines theoretically describe the expected witness-operator values given the actual ramps, not including detection errors or errors due to spontaneous scattering or fluctuations in control parameters. The error bars represent the spread over the observed witness-operator expectations following various global rotation directions of the spins, and indicate the uncertainty due to parasitic effective magnetic fields not appearing in equation (1) as well as possible drifts in the control parameters.

592

weak effective magnetic field, $-B_x \sum \sigma_x^{(i)}$, during the adiabatic evolution²⁵. Figure 4a shows the measured final populations after adiabatic evolution to the Ising Hamiltonian ($|B_y| \ll J_{\text{rms}}$) in the ferromagnetic case without symmetry breaking. Figure 4b shows the same with a symmetry-breaking field, $B_x \approx J_{\text{rms}}$, that breaks the degeneracy of the two components of the ferromagnetic ground state and leaves a dominant $|\uparrow\uparrow\uparrow\rangle$ product state. Figure 4c shows a measurement of the corresponding GHZ witness operator, showing clear quenching of GHZ-type entanglement when symmetry is broken.

For the frustrated antiferromagnetic case, Fig. 4d shows the measured final populations of the evolution of the Ising Hamiltonian, with the six antiferromagnetic states dominating. However, when symmetry is broken (Fig. 4e), the antiferromagnetic system primarily evolves to the three states $|\uparrow\uparrow\downarrow\rangle$, $|\uparrow\downarrow\uparrow\rangle$ and $|\downarrow\uparrow\uparrow\rangle$, consistent with the expected W state. (The residual population in the other states is attributed to non-adiabatic evolution and a finite value of B_y at the end of the ramp.) We characterize entanglement of the symmetry-broken frustrated antiferromagnetic case by measuring the bipartite spin-squeezing witness operator¹⁷

$$W_{\text{SS}} = \left(\hat{J}_x^2 + \frac{3}{4} \right)^2 - 4(\hat{J}_x)^2 - \left(\hat{J}_y^2 + \hat{J}_z^2 - \frac{3}{2} \right)^2$$

We choose this witness operator because it is less sensitive to experimental errors than the W-state witness operator, W_W (ref. 17). The

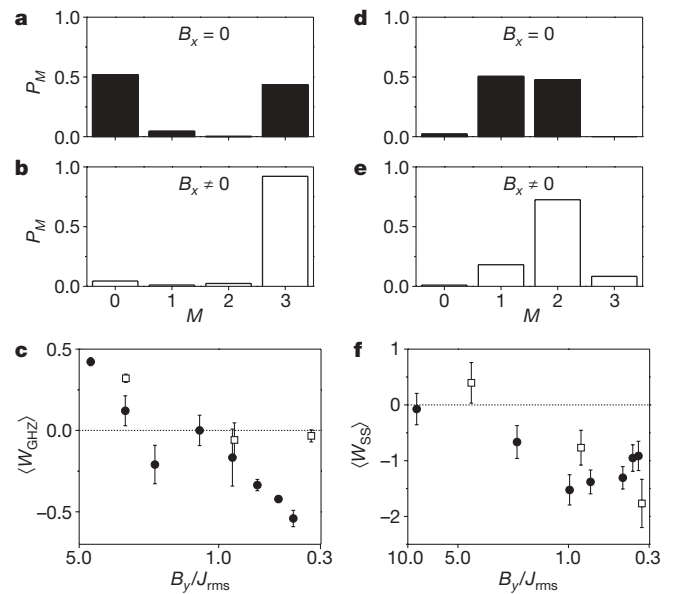


Figure 4 | Entanglement and frustration. The effect of symmetry breaking on the ferromagnetic and antiferromagnetic cases of the Ising model, using a photomultiplier tube for detection. **a**, Measured x -basis populations of ferromagnetic Ising model ($J_1, J_2 < 0$; $B_y/J_{\text{rms}} = 0.42$), expressed in terms of the probability, P_M , of there being M spins in state $|\uparrow\rangle$. **b**, Measured populations of the ferromagnetic Ising model with $B_y/J_{\text{rms}} = 0.34$, where a symmetry-breaking field is added during the ramp and increases linearly to $B_x/J_{\text{rms}} = 0.87$, showing the emergence of the single state, $|\uparrow\uparrow\uparrow\rangle$. **c**, Measurement of the GHZ witness operator without (filled circles) and with (open squares) a symmetry-breaking field, showing a quenching of entanglement. In the presence of a symmetry-breaking field, the direction ϕ of the GHZ witness operator is coordinated with the time-dependent phase of the GHZ state. **d**, Measured x -basis populations of the antiferromagnetic Ising model ($J_1, J_2 > 0$; $B_y/J_{\text{rms}} = 0.36$). **e**, Measured populations of the antiferromagnetic Ising model with $B_y/J_{\text{rms}} = 0.34$, where a symmetry-breaking field is added during the ramp and increases linearly to $B_x/J_{\text{rms}} = 1.19$, showing the emergence of the three states, $|\uparrow\uparrow\downarrow\rangle$, $|\uparrow\downarrow\uparrow\rangle$ and $|\downarrow\uparrow\uparrow\rangle$. **f**, Measurement of the bipartite spin-squeezing entanglement witness operator in the antiferromagnetic case, showing that entanglement remains even after symmetry is broken. As in Fig. 3, the error bars in **c** and **f** represent the uncertainty due to parasitic effective magnetic fields and drifts not appearing in equation (1).

observation of negative values of W_{SS} presented in Fig. 4f shows directly that the frustrated ground state carries entanglement even after global symmetry is broken in the Ising model, and thereby establishes a link between frustration and an extra degree of entanglement.

Simulations of quantum magnetism in this system can be scaled to much larger numbers, N , of trapped ion spins. The stable confinement of larger numbers of ions may require novel ion trap architectures, but there are no known fundamental limitations. As detailed in Supplementary Information, for a fixed level of total laser power the errors associated with decoherence from spontaneous Raman scattering from the lasers is expected to grow only as $N^{1/3}$, holding errors from phonon creation and diabatic transitions to excited states at fixed values. Alternatively, all of these errors can be held at fixed values independent of N as long as the laser power increases as $N^{1/3}$. In either case, however, the required time for adiabatic ramping grows as $N^{1/3}$, so slowly drifting errors such as (real) magnetic fields and motional heating of the ions must be kept under control for very large values of N . This system can also be extended to Heisenberg or XYZ spin models by adding one or two more laser beams^{10,11}. As the system grows, the transverse motional modes that mediate the Ising couplings can give rise to higher levels of frustration and complex phases of magnetic ordering. For instance, by preparing the ground state of a highly frustrated collection of trapped ion spins, it should be possible to create localized topological excitations and guide their transport through the system²⁶. This example of topological matter is of great interest for the robust representation and manipulation of quantum information^{27,28}.

METHODS SUMMARY

The transverse fields are generated through optical stimulated Raman couplings between the spin states, and the Ising couplings are generated through a spin-dependent optical dipole force that is close to resonance with the transverse modes of ion motion^{13,19,20}. Within the Lamb–Dicke regime²³, the result is a nearly pure Ising Hamiltonian of typical coupling strength $J_{rms} \approx 2$ kHz and transverse field up to $B_y \approx 10$ kHz. The relative axes of the Ising coupling and transverse magnetic field in the x – y plane of the Bloch sphere defined in equation (1) are set by the relative phase of the beat notes in the Raman beams. We ramp down the amplitude of the effective magnetic field, B_y , in equation (1) by controlling the optical Raman power, resulting in a typical ramp in Rabi frequency from $\Omega \approx 10$ kHz to 0.3 kHz following an exponential decay trajectory.

Full Methods and any associated references are available in the online version of the paper at www.nature.com/nature.

Received 10 January; accepted 31 March 2010.

1. Wasserman, S. & Faus, K. *Social Network Analysis: Methods and Applications* 98–116 (Cambridge Univ. Press, 1994).
2. Dorogovtsev, S. N., Goltsev, A. V. & Mendes, J. F. F. Critical phenomena in complex networks. *Rev. Mod. Phys.* **80**, 1275–1335 (2008).
3. Bryngelson, J. D. & Wolynes, P. G. Spin glasses and the statistical mechanics of protein folding. *Proc. Natl Acad. Sci. USA* **84**, 7524–7528 (1987).
4. Diep, H. T. *Frustrated Spin Systems* (World Scientific, 2005).
5. Moessner, R. & Ramirez, A. P. Geometrical frustration. *Phys. Today* **59**, 24–29 (2006).
6. Binder, K. & Young, A. P. Spin glasses: experimental facts, theoretical concepts, and open questions. *Rev. Mod. Phys.* **58**, 801–976 (1986).
7. Sachdev, S. *Quantum Phase Transitions* (Cambridge Univ. Press, 1999).

8. Dawson, C. M. & Nielsen, M. A. Frustration, interaction strength, and ground-state entanglement in complex quantum systems. *Phys. Rev. A* **69**, 052316 (2004).
9. Normand, B. & Oles, A. M. Frustration and entanglement in the t_{2g} spin-orbital model on a triangular lattice: valence-bond and generalized liquid states. *Phys. Rev. B* **78**, 094427 (2008).
10. Porras, D. & Cirac, J. I. Effective quantum spin systems with trapped ions. *Phys. Rev. Lett.* **92**, 207901 (2004).
11. Deng, X.-L., Porras, D. & Cirac, J. I. Effective spin quantum phases in systems of trapped ions. *Phys. Rev. A* **72**, 063407 (2005).
12. Friedenauer, A., Schmitz, H., Glueckert, J. T., Porras, D. & Schaetz, T. Simulating a quantum magnet with trapped ions. *Nature Phys.* **4**, 757–761 (2008).
13. Kim, K. *et al.* Entanglement and tunable spin-spin couplings between trapped ions using multiple transverse modes. *Phys. Rev. Lett.* **103**, 120502 (2009).
14. Pauling, L. C. *The Nature of the Chemical Bond* 464–472 (Cornell Univ. Press, 1945).
15. Bramwell, S. T. & Gingras, M. J. P. Spin ice state in frustrated magnetic pyrochlore materials. *Science* **294**, 1495–1501 (2001).
16. Sachdev, S. Order and quantum phase transitions in the cuprate superconductors. *Rev. Mod. Phys.* **75**, 913–932 (2003).
17. Gühne, O. & Toth, G. Entanglement detection. *Phys. Rep.* **474**, 1–75 (2009).
18. Olmschenk, S. *et al.* Manipulation and detection of a trapped Yb^+ hyperfine qubit. *Phys. Rev. A* **76**, 052314 (2007).
19. Mølmer, K. & Sørensen, A. Multiparticle entanglement of hot trapped ions. *Phys. Rev. Lett.* **82**, 1835–1838 (1999).
20. Milburn, G. J., Schneider, S. & James, D. F. V. Ion trap quantum computing with warm ions. *Fortschr. Phys.* **48**, 801–810 (2000).
21. Vaks, V. G., Larkin, A. I. & Ovchinnikov, Y. N. Ising model with interaction between non-nearest neighbors. *Sov. Phys. JETP* **22**, 820–826 (1966).
22. Zhu, S.-L., Monroe, C. & Duan, L.-M. Trapped ion quantum computation with transverse phonon modes. *Phys. Rev. Lett.* **97**, 050505 (2006).
23. Liebfried, D., Blatt, R., Monroe, C. & Wineland, D. Quantum dynamics of single trapped ions. *Rev. Mod. Phys.* **75**, 281–324 (2003).
24. Sackett, C. A. *et al.* Entangled states of trapped atomic ions. *Nature* **404**, 256–259 (2000).
25. Schmitz, H. *et al.* The “arch” of simulating quantum spin systems with trapped ions. *Appl. Phys. B* **95**, 195–203 (2009).
26. Han, Y.-J., Raussendorf, R. & Duan, L.-M. Scheme for demonstration of fractional statistics of anyons in an exactly solvable model. *Phys. Rev. Lett.* **98**, 150404 (2007).
27. Kitaev, A. Fault-tolerant quantum computation by anyons. *Ann. Phys.* **303**, 2–30 (2003).
28. Nayak, C., Simon, S. H., Stern, A., Freedman, M. & Sarma, S. D. Non-Abelian anyons and topological quantum computation. *Rev. Mod. Phys.* **80**, 1083–1159 (2008).

Supplementary Information is linked to the online version of the paper at www.nature.com/nature.

Acknowledgements We acknowledge discussions with J. Moore, M. Newman, J. Wang and S. Das Sarma. This work is supported by US Army Research Office (ARO) award W911NF0710576 with funds from the Defense Advanced Research Projects Agency Optical Lattice Emulator programme, the Intelligence Advanced Research Projects Agency under ARO award W911NF0410234, the US National Science Foundation (NSF) Physics at the Information Frontier programme and the NSF Physics Frontier Center at the Joint Quantum Institute.

Author Contributions All of the authors contributed equally to this work: experimental work was performed by K.K., M.-S.C., S.K., R.I., E.E.E. and C.M.; and theoretical work was performed by J.K.F., G.-D.L. and L.-M.D.

Author Information Reprints and permissions information is available at www.nature.com/reprints. The authors declare no competing financial interests. Readers are welcome to comment on the online version of this article at www.nature.com/nature. Correspondence and requests for materials should be addressed to K.K. (khkim@umd.edu).

METHODS

Transverse field and Ising couplings. The transverse fields are generated through optical Raman couplings between the spin states. Laser radiation red-detuned ~ 1.8 THz from the $^2S_{1/2}-^2P_{1/2}$ transition in $^{171}\text{Yb}^+$ (wavelength, ~ 369.5 nm) uniformly illuminates the ions with an intensity of $\sim 10^3$ W cm $^{-2}$. The laser carries an optical beat note at the $^{171}\text{Yb}^+$ hyperfine splitting frequency, ν_{HF} , generated by electro-optic and acousto-optic modulators²⁹. The effective transverse field, B_y , arises from the resulting resonant carrier transitions²³. We observe Rabi frequencies up to $\Omega \approx 1$ MHz that are stable over time and isotropic over the ions to better than 1%.

The Ising couplings are generated through a spin-dependent force in the x direction at frequency μ (refs 19, 20). The same laser as described above is split into two beams that propagate at right angles to each other with their wavevector difference, k , pointing along the x axis of transverse motion. Two frequencies simultaneously drive an acousto-optic modulator on one of the beam lines in the ‘phase-sensitive’ configuration²⁹, forming bichromatic beat notes at $\nu_{\text{HF}} \pm \mu$. When μ is in the neighbourhood of the x -transverse motional mode frequencies, there is an off-resonance coupling to upper and lower motional side-band transitions²³ of all x -transverse modes simultaneously¹³. However, the detuning, μ , is set far enough from each normal mode that the motion is only virtually excited^{19,20}. The probability of phonon population in the m th normal mode is $p_{\text{ph}} \approx \sum_m (\eta_{i,m} \Omega)^2 / (\mu - \nu_m)^2$, where $\eta_{i,m} = b_{i,m} \sqrt{\hbar k^2 / 4\pi M \nu_m}$ is the Lamb–Dicke parameter of the i th ion with the m th mode, $b_{i,m}$ is the normal-mode transformation matrix, M is the mass of a single ion¹³ and \hbar is Planck’s constant divided by 2π (the centre-of-mass Lamb–Dicke parameter is $\eta_{i,1} \approx 0.025$). Within the Lamb–Dicke regime²³, the result is a nearly pure spin–spin Hamiltonian with nearest-neighbour and next-nearest-neighbour Ising couplings as plotted in Fig. 1c^{13,22}, with a typical Ising coupling strength of $J_{\text{rms}} \approx 2$ kHz. We expect $p_{\text{ph}} < 2\%$ over all detuning settings in the experiment. This is theoretically verified by numerical integration of the Schrödinger equation with and without phonon terms, which results in no observable difference in the evolution shown in Fig. 2b–f. (However, the residual phonon population is expected to contribute a $\sim 2\%$ fidelity degradation for the data shown in Fig. 3a.)

The relative axes of the Ising coupling and transverse magnetic field in the x – y plane of the Bloch sphere defined in equation (1) are set by the relative phase of the radio-frequency sources driving the acousto-optic modulators for the transverse field and Ising couplings as described above. These radio-frequency phases are carefully calibrated by observing appropriate spin dynamics in a series of diagnostic Ramsey experiments¹².

Adiabatic ramping procedure. We ramp down the amplitude of the effective magnetic field, B_y , in equation (1) by controlling the amplitude of the radio-frequency signal driving the acousto-optic modulators, resulting in a typical ramp in Ω from ~ 10.0 kHz to ~ 0.3 kHz. We expect the differential a.c. Stark shift between the $|\uparrow\rangle_z$ and $|\downarrow\rangle_z$ states to change by less than ~ 2 Hz during the ramp. The ramp profile follows an exponential decay in time plus a non-zero offset field, with the characteristic decay time of $35 \mu\text{s}$ chosen as a compromise between non-adiabatic evolution when the ramp is too fast and decoherence effects when the ramp is too slow. Non-adiabatic evolution including imperfect ground-state preparation is expected to contribute population errors at a level below 7%. We observe that the probability of spontaneous scattering from the off-resonance Raman lasers at full power is approximately 15% after a typical simulation time of 0.3 ms. Heating of the motional modes is less than 1 phonon ms $^{-1}$ and does not contribute to significant levels of decoherence. The net effect of these errors is consistent with the data in Figs 2–4. Non-adiabatic evolution is expected to occur when the ramp decay rate is much larger than the gap between the ground and excited spin states, a condition that depends on the form of the transverse Ising model in equation (1). The ramp decay rate is therefore never much larger than $4\pi(|J_1| + |J_2|)$, which sets the scale for the gaps in the ferromagnetic and anti-ferromagnetic cases central to the experiment. However, the ramp does not always resolve ground states separated by gaps of order $|J_1| - |J_2|$, as expected between the symmetric/asymmetric antiferromagnetic states in region I and the ferromagnetic/asymmetric-antiferromagnetic states in region III of Fig. 1c. (These unresolved gaps may explain some of the discrepancy between theory and experiment in Fig. 2e, where there seems to be higher sensitivity to parasitic effective magnetic fields along the x or z axes of the Bloch sphere.)

29. Lee, P. J. *et al.* Phase control of trapped ion quantum gates. *J. Opt. B* 7, S371–S383 (2005).